

Al₁₃[−] and B@Al₁₂[−] superatoms on a molecularly decorated substrate

Masahiro Shibuta¹, Tomoya Inoue², Toshiaki Kamoshida², Toyoaki Eguchi³ & Atsushi Nakajima ^{1,2✉}

Aluminum nanoclusters (Al_n NCs), particularly Al₁₃[−] (*n* = 13), exhibit superatomic behavior with interplay between electron shell closure and geometrical packing in an anionic state. To fabricate superatom (SA) assemblies, substrates decorated with organic molecules can facilitate the optimization of cluster–surface interactions, because the molecularly local interactions for SAs govern the electronic properties via molecular complexation. In this study, Al_n NCs are soft-landed on organic substrates pre-deposited with *n*-type fullerene (C₆₀) and *p*-type hexa-*tert*-butyl-hexa-*peri*-hexabenzocoronene (HB-HBC, C₆₆H₆₆), and the electronic states of Al_n are characterized by X-ray photoelectron spectroscopy and chemical oxidative measurements. On the C₆₀ substrate, Al_n is fixed to be cationic but highly oxidative; however, on the HB-HBC substrate, they are stably fixed as anionic Al_n[−] without any oxidations. The results reveal that the careful selection of organic molecules controls the design of assembled materials containing both Al₁₃[−] and boron-doped B@Al₁₂[−] SAs through optimizing the cluster–surface interactions.

¹Keio Institute of Pure and Applied Sciences (KiPAS), Keio University, 3-14-1 Hiyoshi, Kohoku-ku, Yokohama 223-8522, Japan. ²Department of Chemistry, Faculty of Science and Technology, Keio University, 3-14-1 Hiyoshi, Kohoku-ku, Yokohama 223-8522, Japan. ³Department of Physics, Graduate School of Science, Tohoku University, 6-3 Aramaki Aza-Aoba, Aoba-ku, Sendai 980-8578, Japan. ✉email: nakajima@chem.keio.ac.jp

Through the deposition of size-selected atomic clusters consisting of a few to thousands of atoms on well-defined substrates, nanostructured surfaces can be produced through bottom-up fabrication, which is a promising method for creating low-dimensional nanomaterials with atomic-scale structural precision^{1–4}. The properties of functionalized nanostructured surfaces can be controlled by designing cluster–surface interactions, which facilitates a nanoscale approach to developing nanomaterial-based modified electrodes for application in electrochemistry⁵. The cluster–surface interaction is a fundamental characteristic of such nanostructured materials^{3,6}, and has been a focus in the preparation of heterogeneous catalysts through control of the physical and chemical properties, size, and dimensionality^{7–10}. For example, Haruta indicated the importance of choosing a substrate in enhancing the catalytic activity of gold (Au) nanoparticles for low-temperature CO oxidation⁷. In addition, the substrate acidity has been reported to control the catalytic activity of size-selective platinum (Pt) clusters¹⁰. In these studies, localized cluster–surface interactions are enhanced using metal oxide substrates^{8,9} to avoid the generation of weakly bound nanoclusters (NCs) on a clean surface, because these NCs generally behave as a two-dimensional gas, ultimately resulting in aggregation⁶.

Interactions that take place through charge transfer (CT), or more explicitly, electron transfer¹¹, are important in chemical reactions between two reactant molecules since they lead to the formation of intermolecular CT complexes that exhibit a new electronic transition known as a CT band¹². Their segregated stacking can lead to molecular electrical conductivity, including superconductivity^{13,14}. Such CT processes play an important role in cluster–surface interactions. More specifically, due to the CT interactions with pre-deposited organic molecules on a substrate, the NCs can exist in a monodisperse state on the surface^{15,16}.

Among various gas phase NCs and their characteristic functionalities explored during the past several decades, NCs formed with a highly symmetrical geometry and an electronically closed shell are known as “superatoms” (SAs), which mimic the chemical properties of atoms with clusters^{17–25}. In particular, anionic aluminum (Al) NCs with 13 atoms, i.e., Al_{13}^- , are promising candidates for the fabrication of SA assembled nanomaterials^{26–31}, because Al_{13}^- simultaneously satisfies both icosahedral packing and the electronic shell closing^{32,33} of 40 electrons as $(1\text{S})^2(1\text{P})^6(1\text{D})^{10}(2\text{S})^2(1\text{F})^{14}(2\text{P})^6$, thereby facilitating the bottom-up fabrication of nanostructures with desired functionalities, similar to the case of building nanoblocks^{34–36}.

In this study, we show that the choice of organic substrate can allow molecular control of the CT interactions at the cluster–surface interface and stabilize SAs on the surface. Since the localized interactions between the pre-decorated organic molecules and the deposited NCs are enhanced compared to those of a clean bulk metal or semiconductor substrate, the organic substrate is key to immobilization of the deposited NCs, in which the NC aggregation caused by two-dimensional gas behaviors is suppressed^{16,25}. Thus, we deposit Al_{13}^- and boron-doped B@Al_{12}^- SAs^{17,26,37,38} on organic substrates of *n*-type C_{60} and *p*-type hexa-*tert*-butyl-hexa-*peri*-hexabenzocoronene (HB-HBC, $\text{C}_{66}\text{H}_{66}$ (see Supplementary Fig. 1 and Supplementary Note 1)). Spectroscopic characterization by X-ray photoelectron spectroscopy (XPS) and oxidative reaction measurements of the Al_{13}^- and B@Al_{12}^- SAs on the organic substrates are then conducted to reveal that superatomic behavior can be observed on the *p*-type organic substrates through CT interactions.

Results

Charge state of the Al_n NCs on *n*-type C_{60} and *p*-type HB-HBC substrates. Through magnetron sputtering (MSP) of the Al targets, the generated Al_n^- NCs possessed a mass-to-charge ratio

(m/z) predominantly in the range of 200–800 (see Supplementary Fig. 2). With an ion current of 300 pA, samples containing 2.9×10^{13} mass-selected NCs (~0.6 monolayers (MLs)) could be prepared within 3 h (see “Methods” section and Supplementary Note 2). The morphology of the deposited NCs on the organic substrate was confirmed by scanning tunneling microscopy (STM) imaging^{16,25}, wherein the SAs were found to be monodispersively immobilized without aggregation (see Supplementary Fig. 3).

Figure 1a, b show the XPS spectra around Al 2*p* core levels for (a) Al_{13} on C_{60} and (b) Al_{13} on HB-HBC before (lower) and after (upper) O_2 exposure, respectively. The binding energies (BEs) of Al 2*p*_{3/2} for the bulk Al (Al^0) and oxidized Al (Al^{3+}) have been previously reported (marked by vertical bars in the figure)³⁹. As can be seen, without O_2 exposure, the Al atoms on the C_{60} substrate are completely oxidized, while the Al atoms on HB-HBC are not oxidized. Following O_2 exposure, the Al atoms on C_{60} remain unchanged, while Al atoms on HB-HBC are oxidized to Al^{3+} . As shown in Fig. 1c, d, the corresponding O 1*s* component can be observed in the lower trace of Fig. 1c even without O_2 exposure. These results show that the Al_{13} NCs present on the C_{60} substrate are so reactive that the nascent NCs are oxidized after deposition by some residual gas in the vacuum chamber ($<10^{-5}$ Pa) during the deposition process.

The contrasting oxidation behavior of these two systems correlates well with the C 1*s* XPS peaks from the underlying C_{60} or HB-HBC on highly oriented pyrolytic graphite (HOPG), where the C 1*s* signals are mainly derived from the topmost molecular layer (Fig. 1e, f). As shown in Fig. 1e, after the deposition of Al_{13} on C_{60} , the C 1*s* peak shifts toward a lower BE by ~0.30 eV. Although Al_{13} is nascently oxidized, the shift to a lower BE shows that an anionic C_{60}^- state is formed by Al_{13} oxides through a CT interaction^{16,40}; the degree of shift corresponds well to the formation of C_{60}^- as reported in the literature⁴¹ (see Supplementary Note 3 and Supplementary Fig. 4). A similar C 1*s* shift has been reported when the alkali-like Ta@Si_{16} SA²⁵ is deposited on C_{60} , wherein a shift attributable to $\text{Ta@Si}_{16}^+\text{C}_{60}^-$ is observed^{40,41}, as denoted in Fig. 1e. More quantitatively, when the C_{60} -derived C 1*s* peak is deconvoluted into two peak components corresponding to C_{60} alone (non-interacted) and bound with the Al_n oxide (interacted), the BE of the interacted C_{60} peak is 0.33 eV lower than that of non-interacted C_{60} (Supplementary Fig. 4). In addition to Al_{13} , the Al_7 NCs deposited on C_{60} is nascently oxidized, as can be observed from the Al 2*p* XPS spectrum, although Al_7^+ is regarded to complete the 2*S* shell (i.e., $20 e^-$)²¹. In contrast, after the deposition of 0.6 MLs of Al_{13} on the HB-HBC substrate, the C 1*s* peak shown in Fig. 1f shifts toward a higher BE by ~0.25 eV. Since a similar behavior can be observed for the deposition of the halogen-like Lu@Si_{16} SA²⁵ onto HB-HBC, this shift suggests the formation of a cationic HB-HBC⁺ state, and in turn, an $\text{Al}_{13}^-/\text{HB-HBC}^+$ CT complex.

In addition to Al_{13}^- , all Al_n^- NCs ($n = 7–24$) can be size-selectively deposited onto C_{60} and HB-HBC substrates. More specifically, the Al 2*p* XPS spectra show that these Al_n NCs were successfully deposited onto HB-HBC without undergoing any oxidation reactions (see Supplementary Fig. 5). However, complete oxidation was observed for the Al_n NCs deposited on C_{60} . It should be emphasized that this contrast in the reactivity of Al_n results from the different types of organic substrate molecules, i.e., *n*-type and *p*-type for C_{60} and HB-HBC, respectively. In the Al 2*p* XPS spectra for the Al_n NCs on HB-HBC, peaks were observed in the range of 73.0–73.2 eV, which is close to the peak position for bulk Al (i.e., 73.0 eV)³⁹ (see Supplementary Fig. 6). In addition, the small size dependence is consistent with that in the Al 2*p* core-level BEs for Al_n^+ ($n = 12–15$) obtained from the soft X-ray photoionization efficiency curves⁴². More precisely, the

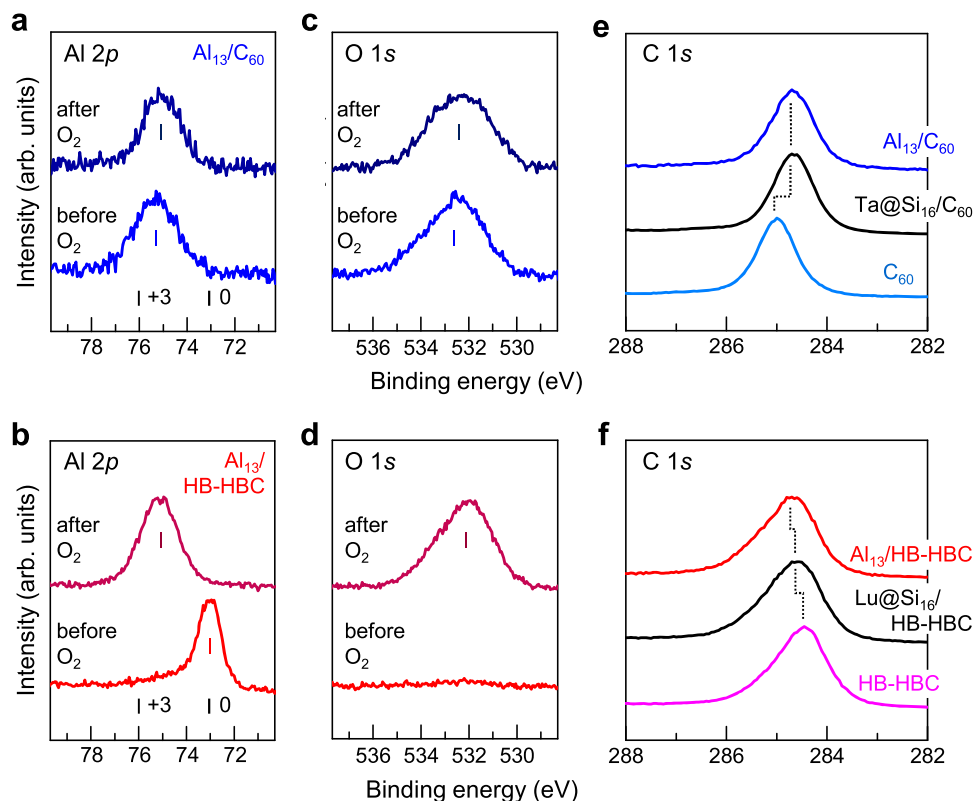


Fig. 1 XPS spectra for Al_{13} on the C_{60} and HB-HBC substrates. **a–d** XPS spectra around the Al 2p core levels for **a** Al_{13} on C_{60} and **b** Al_{13} on HB-HBC before (lower) and after (upper) O_2 exposure (at 5×10^{10} Langmuir ($L = 1.33 \times 10^{-4}$ Pa·s)), along with **c, d** the O 1s spectra for each state. **e, f** The XPS spectra around the C 1s core level for the underlying **e** C_{60} and **f** HB-HBC are also shown for the deposition of Al_{13} and Ta@Si_{16} or Lu@Si_{16} . Reference binding energies (BEs) of Al 2p_{3/2} for the bulk Al (Al^0 and Al^{3+}) and O 1s (O^{2-}) are marked by vertical bars. The BEs for Al 2p show zerovalent Al^0 only for Al_{13} on the HB-HBC substrate before O_2 exposure, while the other BEs are in the vicinity of Al^{3+} . After the deposition of 0.6 ML Al_{13} (blue) or Ta@Si_{16} (black) on C_{60} , the C 1s peak in (**e**) shifts by -0.3 eV toward a lower BE from that before deposition (light blue), indicating the presence of an anionic C_{60}^- state. After the deposition of 0.6 ML Al_{13} (red) or Lu@Si_{16} (black) on HB-HBC, the C 1s peak in (**f**) shifts by -0.25 eV toward a higher BE from that before deposition (pink), indicating the presence of a cationic HB-HBC⁺ state.

charge states of the Al atoms for the deposited Al_n NCs can be discussed in terms of their Al 2p peak positions; the BEs of Al 2p for all Al_n NCs are slightly higher than that of the bulk Al (zerovalent Al^0), suggesting that the Al_n NCs on HB-HBC are anionic rather than neutral. Recently, Kambe et al. have reported the Al 2p XPS spectra for several Al_n species ($n = 4, 12, 13, 28$, and 60) synthesized with dendrimers⁴³, and they revealed a size-dependent behavior in the Al 2p XPS spectra from 71.2 ($n = 4$) to 72.3 eV ($n = 13$) along with a particular shift of more than 0.6 eV between $n = 12$ and 13. However, our Al 2p spectra exhibit a cluster-size dependence within only 0.3 eV for $n = 7$ –24, and no particular peak shift can be observed around $n = 13$. It should be noted here that the peaks in the C 1s XPS spectra for the Al_n NCs on the C_{60} and HB-HBC/HOPG substrates exhibit a similar contrast shift; namely a decrease in the BE for the Al_n NCs on C_{60} (-0.30 eV) and an increase in the BE for the Al_n NCs on HB-HBC ($+0.25$ eV), with a small size-dependent shift being observed (see Supplementary Fig. 7).

Oxidative reactivity of Al_n on the HB-HBC substrate. As shown in Fig. 1b, the Al_n NCs deposited on HB-HBC are oxidized upon O_2 exposure, and the oxidative rates are dependent on the NC size. Figure 2 shows the Al 2p XPS spectra for the Al_{13} on HB-HBC at several different O_2 exposure amounts (i.e., 0 – 5×10^{10} L), where the O_2 exposure amounts (in Langmuir units, $L = 1.33 \times 10^{-4}$ Pa·s) are noted on the right-hand side in of the figure. With increasing the amount of O_2 exposure, the intensity of the peak corresponding

to the zerovalent Al^0 component decreases, while that of the oxidized component Al^{3+} increases along with that of the O 1s component. The oxidative reactivity can therefore be quantitatively evaluated on the basis of its dependence on the O_2 exposure amount from 0 to 1×10^4 L. It should be noted here that at 1×10^4 L O_2 , the Al^0 component survives only in the case of $n = 13$ (Supplementary Fig. 5), which is peculiarly unreactive compared to NCs of other sizes and with Al single crystal surfaces, which are completely oxidized when exposed to 400 L O_2 at room temperature⁴⁴. Furthermore, both the Al 2p and O 1s peaks shift to a lower BE when the O_2 exposure amount is increased from 1×10^4 to 5×10^{10} L, thereby implying that a structural change relevant to a phase transition from amorphous to crystalline Al_2O_3 takes place, such as the formation of α - or γ - Al_2O_3 ⁴⁵.

The chemical reactivity of the Al_n NCs toward O_2 gas was then evaluated based on the oxidation rate, O_{Al_n} , which is a simple index for investigating the size-dependent behavior of the oxidation reaction. More specifically, the peak area ratio, R_{Al_n} , of the non-oxidized component (S_{Al^0}) to the oxidized component ($S_{\text{Al}^{3+}}$) for the Al 2p spectra is plotted against the logarithm of the O_2 exposure amount in L ($\log_{10} \text{O}_2$), and the linear slope is evaluated as O_{Al_n} , where R_{Al_n} is expressed as follows:

$$R_{\text{Al}_n} = \frac{S_{\text{Al}^0}}{S_{\text{Al}^0} + S_{\text{Al}^{3+}}} \quad (1)$$

In this analysis, the oxidation of Al atoms by O_2 is modeled in terms of the dissociative adsorption of O_2 on a single crystal Al

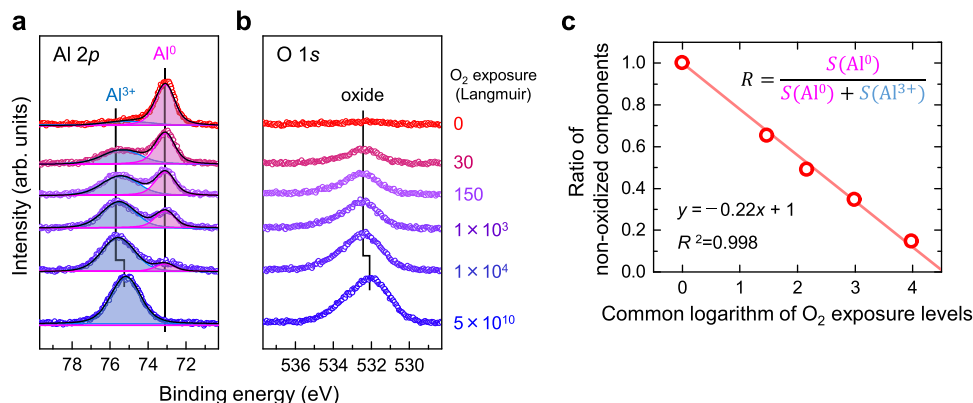


Fig. 2 Oxidative behaviors in the Al 2p and O 1s XPS spectra for Al₁₃ on the HB-HBC substrate. **a, b** XPS spectra around **a** Al 2p and **(b)** O 1s. With increasing O₂ exposure (from top red to bottom blue), the intensity of the zerovalent component (Al⁰) decreases, while those of the oxidized component (Al³⁺) and the O 1s component increase accordingly. **c** The oxidative reactivity is evaluated by the slope of the dependence against the logarithmic O₂ exposure amount from 0 L to 1 × 10⁴ L. At the highest exposure of 5 × 10¹⁰ L, the Al 2p peak shifts to a lower BE, likely due to a structural change relevant to the phase transition of aluminum oxide (see the main text for further details).

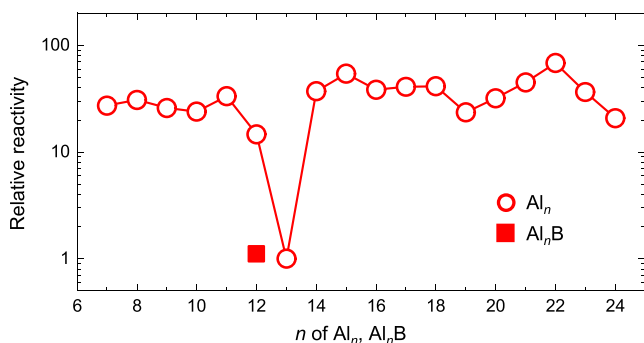
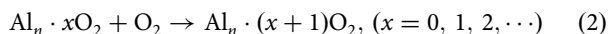


Fig. 3 Size dependent relative reactivities of Al_{*n*} (*n* = 7–24) and B@Al₁₂ on the HB-HBC substrate against the O₂ exposure. The oxidative reactivity rates for Al_{*n*} on the HB-HBC substrate are plotted (red open circles), and a clear local minimum is observed at *n* = 13 along with a small minimum at *n* = 19, while there is no apparent local minimum at *n* = 23. B@Al₁₂ shows a low oxidative reaction rate (red solid square), similar to that of Al₁₃.

surface, whose XPS peak appears at a BE close to that of the Al³⁺ component (i.e., 75–76 eV)⁴⁴.



The oxidation rates, O_{Al_n} , are evaluated by considering the conversion of 1 L → 1 s because the exposure amount can be converted to the corresponding reaction time for elementary reactions. The intersection of the linear line with the x-axis in Fig. 2c gives the O₂ exposure amount of $V_{\text{Al}_{13}}(\text{O}_2)$ that is required to completely oxidize the Al_{*n*} NCs; for Al₁₃, 3.45 × 10⁴ L O₂ is obtained as the value of $V_{\text{Al}_{13}}(\text{O}_2)$. The higher the reactivity, the smaller the quantity of oxygen required to completely oxidize the Al_{*n*} NCs; for example, $V_{\text{Al}_{12}}(\text{O}_2)$ at *n* = 12 is 2.36 × 10³ L O₂, thereby showing that Al₁₂ is 14.6 times more reactive than Al₁₃ (further details regarding the O_{Al_n} and $V_{\text{Al}_n}(\text{O}_2)$ values can be found in Supplementary Note 4 and Supplementary Table 1).

Figure 3 shows the size dependence of the oxidative rates on the Al_{*n*} NCs (*n* = 7–24) deposited on the HB-HBC substrate, where the relative reactivity is evaluated by dividing the $V_{\text{Al}_n}(\text{O}_2)$ value at *n* = 13 by each individual $V_{\text{Al}_n}(\text{O}_2)$ value. A local minimum is clearly found at *n* = 13, and a small local minimum is also found at *n* = 19, while an even–odd alternation relevant to spin conservation⁴⁶ observed in the gas phase reaction^{17,30,47,48} is not obvious. According to previous experimental and theoretical

works^{17,30,38,49–51}, electronically stabilized Al_{*n*} anions should appear at *n* = 19 and 23 as well as at *n* = 13. Since its interactions with HB-HBC induces an anionic character in the deposited Al_{*n*} NCs, Al₁₃ and Al₁₉ complete their 2P (40 e[−]) and 1G (58 e[−]) shells, respectively. However, such stabilization was not observed for Al₂₃ despite this species completing its 3S (70 e[−]) shell (see Fig. 3), and this was attributed to the fact that Al₂₃ is geometrically deformed on the substrate owing to its relatively low rigidity having structural C_s symmetry^{50–52}.

Oxidative reactivity of B@Al₁₂ on the HB-HBC substrate. The structural rigidity of icosahedral Al₁₃[−] is demonstrated by the boron (B) doped B@Al₁₂[−] SAs. Boron belongs to the same group as Al in the periodic table, and it has been reported B@Al₁₂[−] can be preferentially formed as an SA both experimentally and theoretically because the isoelectronic and geometrically small B atom facilitates relaxation of the icosahedral geometric strain when used as a central atom^{37,38,53,54}. Thus, using a B-mixed Al target, B@Al₁₂[−] was formed by MSP and was deposited onto the C₆₀ and HB-HBC substrates (Supplementary Fig. 8).

Figure 4a, b show the XPS spectra around the Al 2p core levels for the B@Al₁₂ deposited on C₆₀ and the B@Al₁₂ deposited on HB-HBC, respectively, before (lower) and after (upper) O₂ exposures, similar to the spectra in Fig. 1. These XPS spectra show that Al atoms on C₆₀ are substantially oxidized without O₂ exposure, but the tailing peak in the Al⁰ region implies that some Al atoms survive without oxidation. In contrast, the Al atoms of B@Al₁₂ deposited on HB-HBC are not oxidized in the same manner as those of Al₁₃, as shown in Fig. 1b.

Upon O₂ exposure, the Al 2p XPS peak for the Al atoms deposited on C₆₀ becomes shaper upon oxidation, while the Al atoms on HB-HBC are sequentially oxidized to Al³⁺. As shown in Fig. 4c, d, the corresponding O 1s component can be observed in the lower trace of Fig. 4c even without O₂ exposure, but the peak intensity is lower than that observed for the Al₁₃ on C₆₀ (see Fig. 1c). In fact, the intensity of the O 1s peak increases with O₂ exposure, as shown in Fig. 4c. These results show that the B@Al₁₂ NCs on C₆₀ are reactive, but that the oxidation rate is suppressed because of the geometrical stabilization induced by B atom encapsulation.

As shown in Fig. 4e, f, the B 1s XPS spectra show the effect of such B atom encapsulation. More specifically, despite a similar oxidative reactivity between the Al and B atoms^{55,56}, the B 1s peak for the B@Al₁₂ on C₆₀ shows that a non-oxidized B⁰

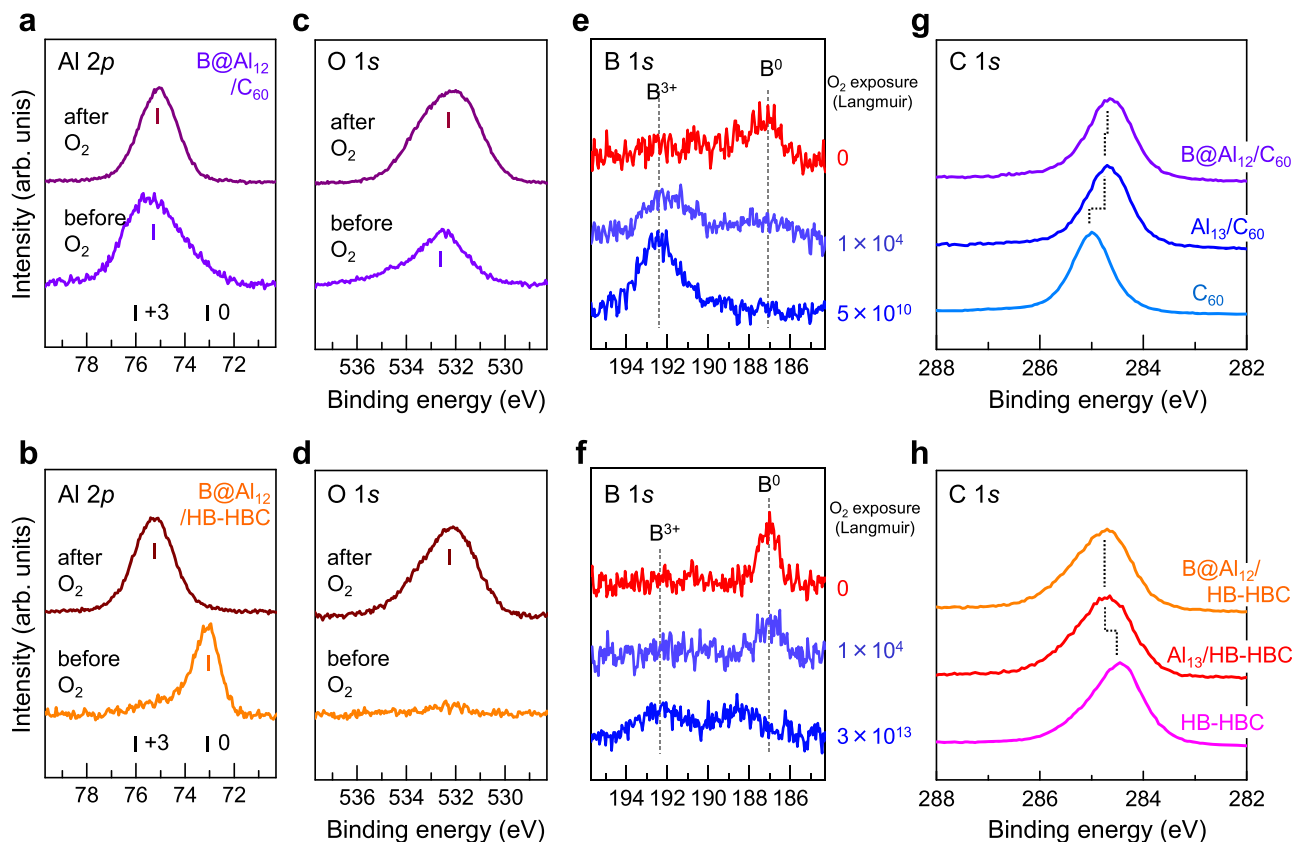


Fig. 4 XPS spectra for B@Al₁₂ on the C₆₀ and HB-HBC substrates. **a–d** XPS spectra around the core Al 2p levels for **a** B@Al₁₂ on C₆₀ and **b** B@Al₁₂ on HB-HBC before (lower) and after (upper) O₂ exposure (at 5 × 10¹⁰ L), along with **c, d** O 1s for each state. **e, f** XPS spectra around the B 1s core levels for **e** B@Al₁₂ on C₆₀ **f** B@Al₁₂ on HB-HBC before (top) and after (lower) O₂ exposure. **g, h** XPS spectra around the C 1s core levels of the underlying **g** C₆₀ or **h** HB-HBC are also shown for the depositions of B@Al₁₂ and Al₁₃. The reference binding energies (BEs) of Al 2p and B 1s for the bulk Al and B (Al⁰/B⁰ and Al³⁺/B³⁺) and O 1s (O^{2−}) are marked by vertical bars. The BEs for Al 2p show the presence of zerovalent Al⁰ only for Al₁₃ on HB-HBC before O₂ exposure, while the other BEs are in the vicinity of Al³⁺, indicating the presence of oxidized Al atoms. After the deposition of 0.6 ML B@Al₁₂ (violet) and Al₁₃ (blue) on C₆₀, the C 1s peak in **(g)** shifts by ~0.3 eV toward a lower BE from that before deposition (light blue), showing an anionic C₆₀[−] state. After the deposition of 0.6 ML B@Al₁₂ (orange) and Al₁₃ (red) on HB-HBC, the C 1s peak in **(h)** shifts by ~0.25 eV toward a higher BE than that before deposition (pink), showing a cationic HB-HBC⁺ state. Importantly, with B atom doping, B@Al₁₂ is stabilized even in the cationic form, as shown by the tailing peak of Al 2p in **(a)** and the non-oxidized B⁰ component in **(e)**.

component can be observed even for the nascent B@Al₁₂ on C₆₀, showing that the oxidation of B atoms to achieve the B³⁺ state is significantly slower than the corresponding oxidation of Al atoms under O₂ exposure. More importantly, the B 1s peak for the B@Al₁₂ on HB-HBC can be observed at an O₂ exposure amount up to ~1 × 10⁴ L, at which point the majority of Al atoms are oxidized. Furthermore, Fig. 4g, h show the C 1s XPS spectra of B@Al₁₂ on the C₆₀ and HB-HBC substrates, respectively, wherein a behavior similar to that of Al₁₃ deposition can be observed. More specifically, for the B@Al₁₂ on C₆₀, the C 1s peak (Fig. 4g) shifts toward a lower BE by ~0.25 eV, while for the B@Al₁₂ on HB-HBC, the C 1s peak (Fig. 4h) shifts toward a higher BE by ~0.25 eV, suggesting the formation of a B@Al₁₂[−]/HB-HBC⁺ CT complex.

When the oxidation rate of B@Al₁₂ is similarly evaluated based on the peak area ratio of the non-oxidized component (S_{Al^0}) to the oxidized component ($S_{Al^{3+}}$) (see Supplementary Fig. 9), the $O_{B@Al_{12}}$ value is the same with the $O_{Al_{13}}$ value within experimental uncertainties, resulting in similar $V_{B@Al_{12}}(O_2)$ and $V_{Al_{13}}(O_2)$ values, as plotted in Fig. 3. Upon B atom encapsulation, all Al atoms become surface Al atoms of the Al₁₂ cage, while in contrast, Al₁₃ consists of twelve surface Al atoms and one central Al atom. The same oxidative rates observed for B@Al₁₂ and Al₁₃ therefore indicate that B@Al₁₂ is more robust because these

equivalent rates were obtained despite the contribution of the central Al atom of Al₁₃.

Theoretical calculations on the charge distributions for the 13-mer anions and cations. For Al₁₃[−], B@Al₁₂[−], Al₁₃⁺, and B@Al₁₂⁺, although theoretical calculations have been reported by several groups^{36,38,57,58}, density functional theory (DFT) calculations are collectively performed to explain the different oxidation behaviors observed for Al₁₃/B@Al₁₂ on the C₆₀ and HB-HBC substrates. The results are presented in Fig. 5, and the Cartesian coordinates are summarized in Supplementary Table 4. For the equilibrium structures, the averaged Al–Al bond lengths are 0.2794 nm for icosahedral Al₁₃[−] and 0.2675 nm for icosahedral B@Al₁₂[−]. The shortened Al–Al bond in B@Al₁₂[−] is ascribed to relaxed geometric strains due to the presence of a small central B atom inside the Al₁₂ cage. For both Al₁₃⁺ and B@Al₁₂⁺, the structural symmetry is lowered, giving C₁ symmetry for Al₁₃⁺ and C_i symmetry for B@Al₁₂⁺, and this was attributed to the electron deficiency of 2P shell closure.

In terms of the charge distributions of Al₁₃[−]/B@Al₁₂[−] and Al₁₃⁺/B@Al₁₂⁺, natural population analysis (NPA) shows that the central Al/B atom is negatively charged, while the surface Al atoms (ρ (Al)) have a positive charge of +0.06/+0.15 for

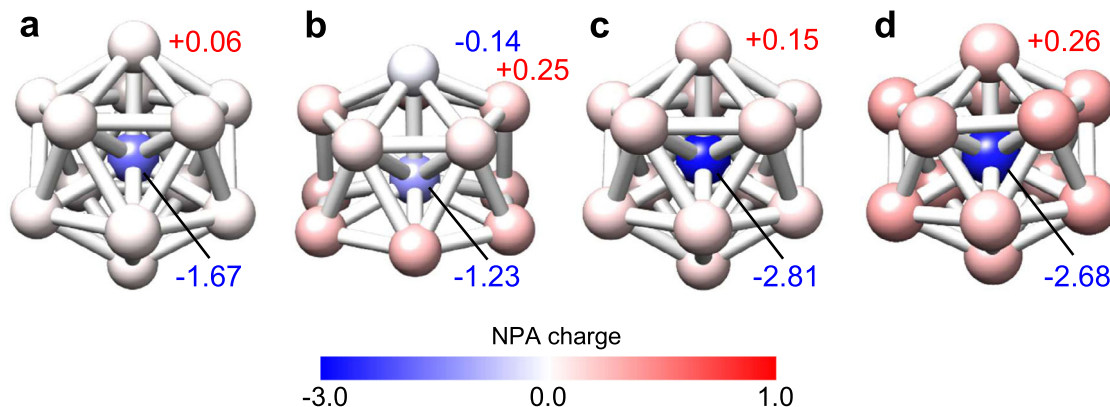


Fig. 5 Calculated NPA charge distributions for Al_{13} and B@Al_{12} . **a–d** Natural population analysis (NPA) distributions for **a** Al_{13}^- , **b** Al_{13}^+ , **c** B@Al_{12}^- , and **d** B@Al_{12}^+ for the optimized structures using PBE0 with 6-311+G(d) for Al_{13}^- and B@Al_{12}^- or with 6-311G(d) for Al_{13}^+ and B@Al_{12}^+ . Along with the representative values, the charge amount is expressed by the color gradation: positive in red and negative in blue. The icosahedral I_h symmetries for Al_{13}^- and B@Al_{12}^- are lowered to C_1 for Al_{13}^+ and C_i for B@Al_{12}^+ owing to electron deficiency in the 2P shell. In general, a central Al/B atom is negatively charged, while the surface Al atoms are positively charged, with the exception of a top Al atom in the distorted Al_{13}^+ in (b).

$\text{Al}_{13}^-/\text{B@Al}_{12}^-$. Compared to the central Al atom ($\rho(\text{Al}) = -1.67$), the central B atom is more negatively charged ($\rho(\text{B}) = -2.68$), and the surrounding twelve Al atoms ($\rho(\text{Al}) = +0.15$) are more positively charged than those in Al_{13}^- ($\rho(\text{Al}) = +0.06$). For $\text{Al}_{13}^+/\text{B@Al}_{12}^+$, the positive charges are delocalized over all Al atoms in the cluster, with the exception of one negatively charged Al atom. Therefore, these theoretical calculations show common electronic features wherein the negatively charged central atoms are masked by the surrounding Al atoms.

Discussion

Charge state of the $\text{Al}_{13}/\text{B@Al}_{12}$ deposited on a p -type substrate and reaction mechanism. The charge states of the deposited $\text{Al}_{13}/\text{B@Al}_{12}$ SAs were found to be significantly influenced by the cluster–surface interactions, which in turn are affected by the molecular character of the organic substrate. More specifically, the p -type organic substrate of HB-HBC was found to electronically stabilize the halogen-like $\text{Al}_{13}/\text{B@Al}_{12}$ NCs on the surface by donating an electron, which led to electron shell closure.

The ultraviolet photoelectron spectroscopy (UPS) reveals the electronic states of the organic substrates (see the UPS spectrum for HB-HBC in Supplementary Fig. 10). More specifically, before the deposition of Al_n , the HOMO energies of the C_{60} and HB-HBC are 2.3 eV⁵⁹ and 1.6 eV (at the peak maximum) below the Fermi level (E_F), respectively. In addition, the LUMO levels can be accessed by two-photon photoemission spectroscopy; LUMO energies of C_{60} and HB-HBC are 0.7 eV⁵⁹ and 1.4 eV above the E_F for C_{60} and HB-HBC, respectively (see Supplementary Fig. 11). These HOMO and LUMO energies indicate that C_{60} (HB-HBC) can be regarded as n -type (p -type) substrates, wherein C_{60} accepts an electron to its LUMO, while HB-HBC donates an electron from its HOMO. Indeed, the quantitative evaluations carried out for the energetics of CT complexation between $\text{Al}_{13}/\text{B@Al}_{12}$ and $\text{C}_{60}/\text{HB-HBC}$ reasonably explain the formation of $\text{Al}_{13}^+\text{C}_{60}^-/\text{B@Al}_{12}^+\text{C}_{60}^-$ and $\text{Al}_{13}^-\text{HB-HBC}^+/\text{B@Al}_{12}^-\text{HB-HBC}^+$ (see Supplementary Note 5 and related contents, i.e., Supplementary Fig. 12, Supplementary Table 2, and Supplementary Table 3).

In the context of O_2 chemisorption on the surfaces, the adsorbed O_2 molecules with two unpaired electrons accept an electron from the surface, forming superoxide (O_2^-) or peroxide (O_2^{2-}) ions^{60,61}. Furthermore, the adsorption energy of two O atoms is larger than the dissociation energy of a single O_2

molecule⁶², and therefore, O atoms are preferentially bound to the surface via a dissociative electron attachment process⁶¹. When O_2 molecules react with CT complexes on a substrate, the O_2 molecules preferentially attack the electron-rich sites of the anions. At the deposition of $\text{Al}_{13}^-/\text{B@Al}_{12}^-$ SAs onto the C_{60} and HB-HBC substrates, as mentioned above, an electron transfer takes place to form $\text{Al}_{13}^+\text{C}_{60}^-/\text{B@Al}_{12}^+\text{C}_{60}^-$ on C_{60} and $\text{Al}_{13}^-\text{HB-HBC}^+/\text{B@Al}_{12}^-\text{HB-HBC}^+$ on HB-HBC. Comparing the electron affinities (E_A s) of the C_{60} (2.68 eV)⁶³ and $\text{Al}_{13}/\text{B@Al}_{12}$ SAs (3.1–3.6 eV)^{33,64,65}, it is easier to transfer an electron from C_{60}^- to O_2 than from $\text{Al}_{13}^-/\text{B@Al}_{12}^-$. In other words, C_{60}^- , which is generated by the deposition of $\text{Al}_{13}/\text{B@Al}_{12}$, facilitates the dissociative electron attachment of O_2 , resulting in the immediate oxidation of $\text{Al}_{13}^+/\text{B@Al}_{12}^+$ cations with O_2^- or O^- through a Coulombic attraction. Therefore, the SA nature of $\text{Al}_{13}^-/\text{B@Al}_{12}^-$ is reinforced by p -type molecular decoration, which renders it possible to fabricate assembled surfaces of chemically robust Al-based SAs.

To conclude, we have successfully characterized the series of Al_n NCs deposited on an n -type C_{60} and p -type HB-HBC substrates. The XPS results reveal that the n -type C_{60} substrate possessing a high E_A withdraws an electron from the Al_n NCs, resulting in a deviation from the electron shell closure. In contrast, the p -type HB-HBC substrate donates one electron to the Al_n NCs, generating electronically stable $\text{Al}_{13}^-/\text{B@Al}_{12}^-$ SAs ($40 e^-$). The chemical stabilities of the deposited Al_n , examined by step-by-step O_2 exposure are shown to be significantly influenced by their charge states on the surface, wherein the stability is enhanced in the $40 e^-$ systems of $\text{Al}_{13}/\text{HB-HBC}$ and $\text{B@Al}_{12}/\text{HB-HBC}$ along with icosahedral rigidity.

Overall, we have demonstrated the importance of optimizing the cluster–surface interactions to achieve stable depositions of $\text{Al}_{13}^-/\text{B@Al}_{12}^-$ SAs. It has also been demonstrated that the molecular decoration of a substrate aids in controlling the local electronic state through the generation of such cluster–surface interactions. We believe that this molecular strategy for the stable deposition of $\text{Al}_{13}/\text{B@Al}_{12}$ could facilitate the fabrication of SA assemblies for all functional SAs generated in the gas phase.

Methods

Sample preparation. The samples of Al_n or Al_nB_m NCs deposited on organic C_{60} and HB-HBC substrates were prepared in an integrated vacuum chamber, including an MSP source, NC deposition, organic evaporation, and photoelectron spectroscopy systems^{16,40,41}. The organic C_{60} and HB-HBC substrates were prepared on cleaned HOPG by thermal evaporation in ultrahigh vacuum (UHV) conditions ($<3 \times 10^{-8}$ Pa). The thicknesses were controlled at 2 and 5 MLs for C_{60}

and HB-HBC, respectively, and were monitored using a quartz crystal microbalance. Commercially available C_{60} (Aldrich, sublimed, 99.9%) was used, while HB-HBC was synthesized (see Supplementary Note 1)⁶⁶.

Anionic Al clusters (Al_n^-) were generated using an MSP system (Ayabo Corp. nanojima-NAP-01)²⁵, in which the Al targets were sputtered with Ar^+ ions in the MSP aggregation cell. After clustering atomic Al vapors into Al_n^- in a cooled (77 K) He gas flow, the Al_n^- NCs were introduced into a quadrupole (Q) mass filter (Extrel CMS; MAX-16000) through ion optics. The production conditions were optimized by monitoring the mass spectra of Al_n^- (see Supplementary Fig. 2) to maximize the ion intensities at the chosen m/z ratios. The mass-selected Al_n^- NCs were then deposited on the C_{60} and HB-HBC substrates with a mass resolution of $m/\Delta m \sim 70$, which was sufficient to exclude the co-deposition of minor products with neighboring m/z values (see Supplementary Fig. 2). The collision energy of the Al_n^- ions was controlled by applying a bias voltage to the substrates (typically +5 V), satisfying the soft-landing conditions (<10 eV/cluster). The number of deposited Al_n^- ions was counted as 2.9×10^{13} clusters, where the coverage of Al_n^- on the substrates was estimated as 0.6 MLs, assuming a deposition area of $2.8 \times 10^{13} \text{ nm}^2$ (6 mm in diameter) and an Al_n^- size estimated by a cubic-root interpolation between the sizes of the Al atom ($n = 1$) and the icosahedral Al_n^- ($n = 13$ and 55) (i.e., 0.62 nm for $n = 7$ and 0.98 nm for $n = 24$ in diameter). The estimated coverage was verified by XPS and UPS measurements with the step-by-step deposition of NCs^{40,41}. The deposited samples were transferred to the photoelectron spectroscopy system connected to the cluster deposition system while maintaining UHV conditions. More detailed procedures for sample preparation were described in Supplementary Note 2.

Photoelectron spectroscopy. XPS measurements were performed using an Mg K α ($h\nu = 1253.6 \text{ eV}$) X-ray source. Photoelectrons emitted from the sample surface were collected with a hemispherical electron energy analyzer (VG SCIENTA, R3000) at a detection angle of 45° from the surface normal. The BE was calibrated using the Au 4f core level (84.0 eV). It was ensured that no charging effect was observed during any of the XPS measurements. In the XPS analyses, after subtracting the Shirley background, peak fitting was performed by instrumental broadening determined from the Au 4f peak profile (Voigt function with a full width at half maximum (FWHM) of 1.09 eV; the Gaussian and Lorentzian widths were 0.75 and 0.56 eV, respectively). A He-I discharge lamp ($h\nu = 21.22 \text{ eV}$) was used for the UPS measurements.

To examine the oxidative reactivities of the deposited Al_n^- NCs, the samples were exposed to O_2 . The amount of O_2 exposure was defined as Langmuir units ($L = 1.33 \times 10^{-4} \text{ Pa}\cdot\text{s}$). The O_2 gas was introduced into the XPS/UPS system using a variable leak valve for low exposure levels ($\leq 10^4 L$). At higher exposure levels ($> 10^{10} L$), the sample was exposed to O_2 in a UHV chamber isolated from the XPS/UPS system. All XPS/UPS measurements and O_2 exposures were performed at room temperature.

Density functional theory (DFT) calculations. Geometry optimizations for the Al_{13}^- , $B@Al_{12}^-$, Al_{13}^+ , and $B@Al_{12}^+$ cluster ions with singlet spin states were performed by DFT implemented in the Gaussian 16 program⁶⁷. All equilibrium geometries were optimized until no imaginary frequencies were found. The hybrid exchange-correlation function PBE0^{68,69} was employed at 6-311+G(d) for Al_{13}^- and $B@Al_{12}^-$ and at 6-311G(d) for Al_{13}^+ and $B@Al_{12}^+$. Population analyses were performed using NPA⁷⁰ for the total electron density obtained at the same level of DFT calculations.

Data availability

The data that support the findings of this study can be found in the manuscript, Supplementary information, or are available from the corresponding author upon request.

Code availability

The codes used for the analysis in the current study are available from the corresponding author upon request.

Received: 20 September 2021; Accepted: 17 February 2022;

Published online: 14 March 2022

References

- Cleveland, C. L. & Landman, U. Dynamics of cluster–surface collisions. *Science* **257**, 355–361 (1992).
- Bromann, K. et al. Controlled deposition of size-selected silver nanoclusters. *Science* **274**, 956–958 (1996).
- Landman, U. Materials by numbers: computations as tools of discovery. *Proc. Natl Acad. Sci. USA* **102**, 6671–6678 (2005).
- Johnson, G. E., Gunaratne, D. & Laskin, J. Soft- and reactive landing of ions onto surfaces: concepts and applications. *Mass Spectrom. Rev.* **35**, 439–479 (2016).
- Zhu, C., Yang, G., Li, H., Du, D. & Lin, Y. Electrochemical sensors and biosensors based on nanomaterials and nanostructures. *Anal. Chem.* **87**, 230–249 (2015).
- Popok, V. N., Barke, I., Campbell, E. E. B. & Meiwes-Broer, K.-H. Cluster–surface interaction: From soft landing to implantation. *Surf. Sci. Rep.* **66**, 347–377 (2011).
- Haruta, M. Catalysis of gold nanoparticles deposited on metal oxides. *Cattech* **6**, 102–115 (2002).
- Yoon, B. et al. Charging effects on bonding and catalyzed oxidation of CO on Au_8 clusters on MgO. *Science* **307**, 403–407 (2005).
- Landman, U., Yoon, B., Zhang, C., Heiz, U. & Arenz, M. Factors in gold nanocatalysis: oxidation of CO in the non-scalable size regime. *Top. Catal.* **44**, 145–158 (2007).
- Crampton, A. S., Rötzer, M. D., Landman, U. & Heiz, U. Can support acidity predict sub-nanometer catalyst activity trends? *ACS Catal.* **7**, 6738–6744 (2017).
- Marcus, R. A. Electron transfer reactions in chemistry: theory and experiment (Nobel lecture). *Angew. Chem. Int. Ed.* **32**, 1111–1121 (1993).
- Wang, Y. Photophysical properties of fullerenes/N,N-diethylaniline charge transfer complexes. *J. Phys. Chem.* **96**, 764–767 (1992).
- Akamatsu, H., Inokuchi, H. & Matsunaga, Y. Electrical conductivity of the perylene–bromine complex. *Nature* **173**, 168–169 (1954).
- Yamada, J., Akutsu, H., Nishikawa, H. & Kikuchi, K. New trends in the synthesis of π -electron donors for molecular conductors and superconductors. *Chem. Rev.* **104**, 5057–5084 (2004).
- Duffe, S. et al. Penetration of thin C_{60} films by metal nanoparticles. *Nat. Nanotechnol.* **5**, 335–339 (2010).
- Nakaya, M., Iwasa, T., Tsunoyama, H., Eguchi, T. & Nakajima, A. Formation of a superatom monolayer using gas-phase-synthesized $Ta@Si_{16}$ nanocluster ions. *Nanoscale* **6**, 14702–14707 (2014).
- Castleman, A. W. Jr. & Khanna, S. N. Clusters, superatoms, and building blocks of new materials. *J. Phys. Chem. C* **113**, 2664–2675 (2009).
- Castleman, A. W. Jr. From elements to clusters: the periodic table revisited. *J. Phys. Chem. Lett.* **2**, 1062–1069 (2011).
- Jena, P. Beyond the periodic table of elements: The role of superatoms. *J. Phys. Chem. Lett.* **4**, 1432–1442 (2013).
- Tomalia, D. A. & Khanna, S. N. A Systematic framework and nanoparadigmatic concept for unifying nanoscience: Hard/soft nanoelements, superatoms, meta-atoms, New emerging properties, periodic property patterns, and predictive Mendeleev-like nanoparadigmatic tables. *Chem. Rev.* **116**, 2705–2774 (2016).
- Luo, Z. & Castleman, A. W. Jr. Special and general superatoms. *Acc. Chem. Res.* **47**, 2931–2940 (2014).
- Reber, A. C. & Khanna, S. N. Superatoms: electronic and geometric effects on reactivity. *Acc. Chem. Res.* **50**, 255–263 (2017).
- Jena, P. & Sun, Q. Super atomic clusters: design rules and potential for building blocks of materials. *Chem. Rev.* **118**, 5755–5870 (2018).
- Ferrari, P., Vanbuel, J., Janssens, E. & Lievens, P. Tuning the reactivity of small metal clusters by heteroatom doping. *Acc. Chem. Res.* **51**, 3174–3182 (2018).
- Tsunoyama, H., Shibuta, M., Nakaya, M., Eguchi, T. & Nakajima, A. Synthesis and characterization of metal-encapsulating Si_{16} cage superatoms. *Acc. Chem. Res.* **51**, 1735–1745 (2018).
- Bergeron, D. E., Castleman, A. W. Jr., Morisato, T. & Khanna, S. N. Formation of $Al_{13}I^-$: evidence for the superhalogen character of Al_{13} . *Science* **304**, 84–87 (2004).
- Revels, J. U., Khanna, S. N., Roach, P. J. & Castleman, A. W. Jr. Multiple valence superatoms. *Proc. Natl Acad. Sci. USA* **103**, 18405–18410 (2006).
- Reber, A. C., Khanna, S. N. & Castleman, A. W. Jr. Superatom compounds, clusters, and assemblies: ultra alkali motifs and architectures. *J. Am. Chem. Soc.* **129**, 10189–10194 (2007).
- Pal, R. et al. Probing the electronic and structural properties of doped aluminum clusters: $M Al_{12}^-$ ($M = Li, Cu, \text{ and } Au$). *J. Chem. Phys.* **128**, 024305 (2008).
- Leuchtner, R. E., Harms, A. C. & Castleman, A. W. Jr. Aluminum cluster reactions. *J. Chem. Phys.* **94**, 1093–1101 (1991).
- Yin, B. & Luo, Z. Thirteen-atom metal clusters for genetic materials. *Coord. Chem. Rev.* **400**, 213053 (2019).
- Li, X., Wu, H., Wang, X.-B. & Wang, L.-S. s-p Hybridization and electron shell structures in aluminum clusters: a photoelectron spectroscopy study. *Phys. Rev. Lett.* **81**, 1909–1912 (1998).
- Knight, W. D. et al. Electronic shell structure and abundances of sodium clusters. *Phys. Rev. Lett.* **52**, 2141–2143 (1984).
- Khanna, S. N. & Jena, P. Assembling crystals from clusters. *Phys. Rev. Lett.* **69**, 1664–1667 (1992).
- Claridge, S. A. et al. Cluster-assembled materials. *ACS Nano* **3**, 244–255 (2009).
- Yin, B. & Luo, Z. Coinage metal clusters: from superatom chemistry to genetic materials. *Coord. Chem. Rev.* **429**, 213643 (2021).

37. Nakajima, A., Kishi, T., Sugioka, T. & Kaya, K. Electronic and geometric structures of aluminum-boron negative cluster ions ($Al_nB_m^-$). *Chem. Phys. Lett.* **187**, 239–244 (1991).
38. Akutsu, M. et al. Experimental and theoretical characterization of aluminum-based binary superatoms of $Al_{12}X$ and their cluster salts. *J. Phys. Chem. A* **110**, 12073–12076 (2006).
39. Bianconi, A., Bachrach, R. Z., Hagstrom, S. B. M. & Flodström, S. A. Al- Al_2O_3 interface study using surface soft-x-ray absorption and photoemission spectroscopy. *Phys. Rev. B* **19**, 2837–2843 (1973).
40. Shibuta, M. et al. Chemical characterization of an alkali-like superatom consisting of a Ta-encapsulating Si_{16} cage. *J. Am. Chem. Soc.* **137**, 14015–14018 (2015).
41. Ohta, T., Shibuta, M., Tsunoyama, H., Eguchi, T. & Nakajima, A. Charge transfer complexation of Ta-encapsulating Ta@ Si_{16} superatom with C_{60} . *J. Phys. Chem. C* **120**, 15265–15271 (2016).
42. Walter, M. et al. Experimental and theoretical $2p$ core-level spectra of size-selected gas-phase aluminum and silicon cluster cations: chemical shifts, geometric structure, and coordination-dependent screening. *Phys. Chem. Chem. Phys.* **21**, 6651–6661 (2019).
43. Kambe, T., Haruta, N., Imaoka, T. & Yamamoto, K. Solution-phase synthesis of Al_{13}^- using a dendrimer template. *Nat. Commun.* **8**, 2046 (2017).
44. Martinson, C. W. B. & Flodstrom, S. A. Oxygen adsorption on aluminum single crystal faces studied by AES, XPS and LEED. *Surf. Sci.* **80**, 306–316 (1979).
45. van Heijnsbergen, D., Demyk, K., Duncan, M. A., Meijer, G. & von Helden, G. Structure determination of gas phase aluminum oxide clusters. *Phys. Chem. Chem. Phys.* **5**, 2515–2519 (2003).
46. Burgert, R. et al. Spin conservation accounts for aluminum cluster anion reactivity pattern with O_2 . *Science* **319**, 438–442 (2008).
47. Sweeny, B. C. et al. Thermal kinetics of $Al_n^- + O_2$ ($n = 2–30$): measurable reactivity of Al_{13}^- . *J. Phys. Chem. A* **123**, 6123–6129 (2019).
48. Sweeny, B. C. et al. Redefining the mechanism of O_2 etching of Al_n^- superatoms: an early barrier controls reactivity, analogous to surface oxidation. *J. Phys. Chem. Lett.* **11**, 217–220 (2020).
49. Nakajima, A., Hoshino, K., Naganuma, T., Sone, Y. & Kaya, K. Ionization potentials of aluminum-sodium bimetallic clusters (Al_nNa_m). *J. Chem. Phys.* **95**, 7061–7066 (1991).
50. Aguado, A. & López, J. M. Structures and stabilities of Al_n^+ , Al_m^- and Al_n^- ($n = 13–34$) clusters. *J. Chem. Phys.* **130**, 064704 (2009).
51. Drebov, N. & Ahlrichs, R. Structures of Al_n , its anions and cations up to $n = 34$: a theoretical investigation. *J. Chem. Phys.* **132**, 164703 (2010).
52. Iwasa, T. & Nakajima, A. Geometric, electronic, and optical properties of a boron-doped aluminum cluster of $B_2Al_{21}^-$. *Chem. Phys. Lett.* **582**, 100–104 (2013).
53. Smith, J. C., Reber, A. C., Khanna, S. N. & Castleman, A. W. Jr. Boron substitution in aluminum cluster anions: magic clusters and reactivity with oxygen. *J. Phys. Chem. A* **118**, 8485–8492 (2014).
54. Chauhan, V., Reber, A. C. & Khanna, S. N. Strong lowering of ionization energy of metallic clusters by organic ligands without changing shell filling. *Nat. Commun.* **9**, 2357 (2018).
55. Bauer, S. H. Oxidation of B, BH, BH_2 , and B_mH_n species: thermochemistry and kinetics. *Chem. Rev.* **96**, 1907–1916 (1996).
56. Garland, N. L. & Nelson, H. H. Temperature dependence of the kinetics of the reaction of $Al+O_2 \rightarrow AlO+O$. *Chem. Phys. Lett.* **191**, 269–272 (1992).
57. Gong, X. G. & Kumar, V. Enhanced stability of magic clusters: A case study of icosahedral $Al_{12}X$, $X=B, Al, Ga, C, Si, Ge, Ti, As$. *Phys. Rev. Lett.* **70**, 2078–2081 (1993).
58. Zhao, J., Du, Q., Zhou, S. & Kumar, V. Endohedrally doped cage clusters. *Chem. Rev.* **120**, 9021–9163 (2020).
59. Shibuta, M. et al. Direct observation of photocarrier electron dynamics in C_{60} films on graphite by time-resolved two-photon photoemission. *Sci. Rep.* **6**, 35853 (2016).
60. Höfer, U., Morgen, P., Wurth, W. & Umbach, E. Metastable molecular precursor for the dissociative adsorption of oxygen on Si(111). *Phys. Rev. Lett.* **55**, 2979–2982 (1985).
61. Libisch, F., Huang, C., Liao, P., Pavone, M. & Carter, E. A. Origin of the energy barrier to chemical reactions of O_2 on Al(111): Evidence for charge transfer, not spin selection. *Phys. Rev. Lett.* **109**, 198303 (2012).
62. Toyoshima, I. & Somorjai, G. A. Heats of chemisorption of O_2 , H_2 , CO, CO_2 , and N_2 on polycrystalline and single crystal transition metal surfaces. *Catal. Rev. Sci. Eng.* **19**, 105–159 (1979).
63. Huang, D. L., Dau, P. D., Liu, H. T. & Wang, L. S. High-resolution photoelectron imaging of cold C_{60}^- anions and accurate determination of the electron affinity of C_{60} . *J. Chem. Phys.* **140**, 224315 (2014).
64. Ganteför, G., Gausa, M., Meiwes-Broer, K. H. & Lutz, H. O. Photoelectron spectroscopy of jet-cooled aluminium cluster anions. *Z. Phys. D* **9**, 253–261 (1988).
65. Kawamata, H., Negishi, Y., Nakajima, A. & Kaya, K. Electronic properties of substituted aluminum clusters by boron and carbon atoms ($Al_nB_m^-/Al_nC_m^-$): New insights into s-p hybridization and perturbed shell structures. *Chem. Phys. Lett.* **337**, 255–262 (2001).
66. Rathore, R. & Burns, C. L. A practical one-pot synthesis of soluble hexa-peri-hexabenzocoronene and isolation of its cation-radical salt. *J. Org. Chem.* **68**, 4071–4074 (2003).
67. Frisch, M. J. et al. Gaussian 16 Revision A.03 (Gaussian, Wallingford, CT, USA, 2016).
68. Adamo, C. & Barone, V. Toward reliable density functional methods without adjustable parameters: The PBE0 model. *J. Chem. Phys.* **110**, 6158–6170 (1999).
69. Perdew, J. P., Burke, K. & Ernzerhof, M. Generalized gradient approximation made simple. *Phys. Rev. Lett.* **77**, 3865–3868 (1996).
70. Reed, A. E., Weinstock, R. B. & Weinhold, F. Natural population analysis. *J. Chem. Phys.* **83**, 735–746 (1985).

Acknowledgements

We are grateful to Professor Hideyuki Tsukada (Yokohama City University) for supplying the HB-HBC samples, to Professor Takashi Yokoyama (Yokohama City University) for providing information regarding the molecular deposition of HB-HBC, and to Dr. Hironori Tsunoyama for providing some calculation results. This work is partly supported by JSPS KAKENHI of Grants-in-Aid for Scientific Research (A) No. 19H00890 (A.N.) and Scientific Research (C) No. 18K04942 (M.S.), for Challenging Research Nos. 17H06226(A.N.) and 21K18939 (A.N.), and for Transformative Research Areas (A) “Hyper-Ordered Structures Science” (21H05573) (A.N.).

Author contributions

M.S., T.I., T.K., T. E., and A.N. contributed to the experimental processes. M.S., T.I., and A.N. carried out the simulations and theoretical interpretations. A.N. supervised the overall project. All authors have given approval to the final version of the manuscript.

Competing interests

A.N. is an inventor on JAPAN patent JP 5493139, submitted by the JST agency and Ayabo Corp., which covers a nanocluster generator. The remaining authors declare no competing interests.

Additional information

Supplementary information The online version contains supplementary material available at <https://doi.org/10.1038/s41467-022-29034-9>.

Correspondence and requests for materials should be addressed to Atsushi Nakajima.

Peer review information *Nature Communications* thanks Zhixun Luo and the other, anonymous, reviewer(s) for their contribution to the peer review of this work. Peer reviewer reports are available.

Reprints and permission information is available at <http://www.nature.com/reprints>

Publisher's note Springer Nature remains neutral with regard to jurisdictional claims in published maps and institutional affiliations.



Open Access This article is licensed under a Creative Commons Attribution 4.0 International License, which permits use, sharing, adaptation, distribution and reproduction in any medium or format, as long as you give appropriate credit to the original author(s) and the source, provide a link to the Creative Commons license, and indicate if changes were made. The images or other third party material in this article are included in the article's Creative Commons license, unless indicated otherwise in a credit line to the material. If material is not included in the article's Creative Commons license and your intended use is not permitted by statutory regulation or exceeds the permitted use, you will need to obtain permission directly from the copyright holder. To view a copy of this license, visit <http://creativecommons.org/licenses/by/4.0/>.

© The Author(s) 2022